Oxygen vacancies in cubic ZrO_2 nanocrystals studied by an *ab initio* embedded cluster method

D. Muñoz Ramo,[1,2] P. V. Sushko,[1,3] J. L. Gavartin,[4] and A. L. Shluger[1,3]
[1]*Department of Physics and Astronomy and the London Centre for Nanotechnology, University College London, Gower Street, London WC1E 6BT, United Kingdom*
[2]*Department of Materials Chemistry, The Ångström Laboratory, Uppsala University, Box 538, S-75121 Uppsala, Sweden*
[3]*WPI Advanced Institute for Materials Research, Tohoku University, 2-1-1 Katahira, Aoba, Sendai 980-8577, Japan*
[4]*Accelrys Inc., 334 Cambridge Science Park, Cambridge CB4 0WN, United Kingdom*
(Received 29 July 2008; published 23 December 2008)

We have developed an embedded cluster method for the calculation of the electronic structure and properties of point defects in cubic ZrO_2 nanocrystallites. The accuracy of the method is tested through a detailed comparison of the atomic and electronic structures of the perfect lattice and defect properties with the results of periodic calculations. The optical absorption and magnetic properties of oxygen vacancies with charge states ranging from $+2|e|$ to $-2|e|$ are calculated. Furthermore, the method can be used to study the magnetic, optical, photoluminescence, chemical, and other properties of pure and doped ZrO_2 powders and their mixtures with other materials.

DOI: 10.1103/PhysRevB.78.235432 PACS number(s): 71.55.−i, 71.20.−b, 73.22.−f, 78.67.Bf

I. INTRODUCTION

Zirconia (ZrO_2) is a material of great interest both scientifically and in terms of its technological applications. Its high resistance to thermal shock makes it one of the best refractive materials known. It also exhibits high ionic conductivity at high temperatures once doped with aliovalent oxides such as CaO, MgO, and Y_2O_3. These properties have been exploited in solid oxide fuel cells, catalytic supports, and oxygen gas sensors. Zirconia, along with hafnia, has also been proposed as a replacement for silicon dioxide as a gate layer material in metal-oxide semiconductor devices due to its high dielectric constant and thermal stability under processing conditions.[1,2]

Most applications of ZrO_2 are based on properties of its less stable tetragonal and cubic polymorphs stabilized by either doping or size confinement as in thin films and nanocrystals. The most common method of stabilization is doping with aliovalent cations such as yttrium or calcium (see, for example, Refs. 3–5). More recently, it has been suggested that ZrO_2 nanocrystallites below a certain particle size of the order of 40 nm adopt a cubiclike structure at room temperature (see, for example, Refs. 6–8). The critical particle size and the mechanisms of the cubic phase stabilization are not yet fully established. Recent papers suggest that the particle size below which the cubic phase of pure ZrO_2 is stable is rather less than 5 nm.[9] Factors promoting the stabilization of the better-studied tetragonal phase of ZrO_2 nanoparticles were reviewed recently in Ref. 10 and are most probably also relevant to the cubic phase. Due to the fact that, in nanoparticles, the surface atoms may account for a large or even dominant fraction of all atoms, their phase stability is determined by a fine balance of the bulk and surface energy[11–13] and can be tuned by the surface excess of one of the components of a doped system.[14,15] In most experiments the tetragonal phase of ZrO_2 is thought to be stabilized by the cluster size, and/or by coating [e.g., with MgO (Ref. 14) and Al_2O_3 (Ref. 15)], by doping [e.g., with Ce (Ref. 16)], and by oxygen vacancies, which are always present inside nanoparticles.[15,16] Spectroscopic techniques, such as optical absorption[16] and electron paramagnetic resonance (EPR),[17] can provide useful information about the nature of vacancies[16] and impurities as a function of their position inside nanocrystallites, but the results of these measurements require further theoretical analysis.

Better understanding of the electronic structure, electron and hole trapping, chemical properties, and mechanisms of photoinduced processes in ZrO_2 nanostructures can be achieved using accurate electronic structure computational techniques. In particular, an embedded cluster method (ECM) in conjunction with density-functional theory (DFT) and hybrid density functionals provides the flexibility and accuracy required for studying these complex systems. In this method, a system is partitioned into two coupled subsystems: a *region of interest*, considered quantum mechanically, and its *environment*, considered classically. Similar methods [also known as quantum-mechanical/molecular mechanics (QM/MM) models] have been applied to a wide range of scientific problems in various systems, for example, the structure and reactivity of catalysts and large organic molecules.[18] ECM has been used successfully to study defect properties in crystalline and amorphous SiO_2,[19–21] MgO,[22] CaO,[23] Mg_2SiO_4,[24] HfO_2,[25,26] and $12CaO \cdot 7Al_2O_3$.[27] It has also been applied to the study of defects in MgO nanoparticles and at interparticle interfaces of MgO.[28,29] We note that different types of embedding potential are required for highly ionic materials, such as MgO,[22] and materials with polar bonds, such as SiO_2.[19–21] In this paper we develop a reliable and robust embedded cluster method for ZrO_2 and apply it to study the properties of oxygen vacancies in cubic ZrO_2 nanocrystallites. Furthermore, this method can be used to study the magnetic,[30] photoluminescence,[16] chemical, and other properties of pure and doped ZrO_2 powders and their mixture with CeO_2 and other materials.[14–16,30]

The rest of the paper is organized as follows. First, we describe the details of the embedded cluster method and parametrization developed for cubic ZrO_2 (c-ZrO_2). Then, we present the results obtained for several charged states of the oxygen vacancy and compare our results with experimental

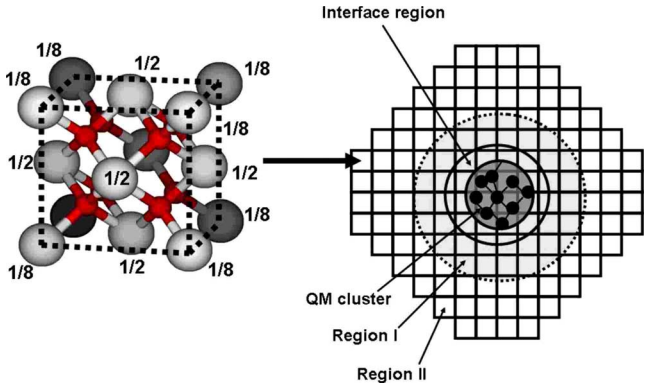

FIG. 1. (Color online) (Left) Schematics of the building block used to generate the nanocluster. Dark small spheres are oxygen atoms and bright large spheres represent Zr atoms. Values next to each Zr center show the fraction of the specific atom contributing to the building block. (Right) General scheme of the embedded cluster model for a nanocrystallite.

data where available. Finally, we discuss the problems with, and limitations of, our approach.

II. EMBEDDED CLUSTER METHOD

In the method described in this section, "region of interest" refers to a region of the system (bulk solid, surface, and nanocrystallite) in which a defect induces a strong modification of the local atomic and electronic structure, while the "environment" provides an embedding potential for it. Many existing QM/MM schemes share common features (see, for example, Ref. 18) but differ in their method of implementation of the short-range embedding potential, long-range polarization of the environment, and the interaction of the QM and MM subsystems.

In our method, the total energy includes the contribution due to the interaction of the QM region with the rest of the host lattice, the ionic and electronic polarization of the lattice by the QM region, and the reciprocal effect of the lattice polarization on the QM region itself. Thus, the electronic structure of the QM region is consistent with the perturbation which it induces on the polarizable environment and vice versa. This scheme is implemented in the computer code GUESS.[31] Below, we describe briefly the implementation of this method for modeling a defect inside a nanocrystal. First, we present a fairly general description of the method and then describe the details of the implementation pertaining to a particular case of vacancies in cubic ZrO_2 nanocrystallites.

A. Nanocrystal and its regions

We consider nanometer-sized nanocrystals, henceforth referred to as NCs. Each NC is constructed from material-dependent building blocks, as discussed below. We note that this technique has flexibility in treating coated nanocrystals and assemblies of similar and different nanocrystals.[28,32]

A NC is divided into two regions: region I, in which a defect or other system of interest is located, and the remainder of the nanocrystal, region II (see Fig. 1). Generally, region I can be located anywhere inside or at the surface of the NC.[29] All atoms in region I are free to relax, and the total energy of the system is minimized with respect to their coordinates, while atoms in region II remain fixed in their lattice positions. Thus, region I represents a polarizable part of the system and region II mimics the infinite (in the case of bulk crystals) or finite (in the case of nanoparticles) environment for atoms in region I.

Region I is divided further into three subregions (Fig. 1): (i) an inner part, which is described quantum mechanically (the "QM cluster"), (ii) an outer part, which is described using the classical shell model,[33] and (iii) an interface region between them. The sizes of region I and of the QM cluster are chosen so as to satisfy several criteria. First, the QM cluster should be large enough to reproduce the main features of the electronic structure of the material and include in full the region in which defect-induced bond breakage and perturbation of the electronic structure take place. Second, region I should be large enough to accommodate the lattice distortion induced by the defect in the QM cluster. Generally, two distinct cases can be considered: (i) the specific NC is modeled in its entirety or (ii) the NC is so large or the defect is so far from its surface that the particular shape and surface structure of the NC is irrelevant. In the latter case, the NC used in calculations should be large enough for region II to mimic accurately the Coulomb and short-range potentials provided by the remaining part of the system. This criterion can be met if the electrostatic potential inside region I converges rapidly with the size of the NC. To achieve this, the nanocluster is constructed from material-specific structural elements, which may differ from lattice unit cells. The structural elements are designed so that their dipole and quadrupole moments are either zero or cancel each other out on average. For example, in the case of MgO a Mg_4O_4 cubic cluster can be such a structural element. In the case of α-quartz SiO_2, a convenient structural element is a $Si(O_{1/2})_4$ tetrahedron,[19–21] while more complex structures have been designed for forsterite (Mg_2SiO_4).[24]

The convergence of the electrostatic potential depends on the shape of the NC; it converges most rapidly for spherical nanoclusters. Much more complex NCs may need to be used in studies of assemblies of nanoparticles, powder grains, and their interfaces.[28,29]

B. QM cluster

A QM cluster should include the region in which the perturbation of the electronic structure and local geometry cannot be described reliably using a classical shell model. In practice, its size is always chosen so as to balance the feasible computational cost with the required accuracy of calculations, which is defined by the method used for calculating the QM contribution to the total energy.

The compactness of the cluster is defined as the ratio $\nu = n_{\text{QM-QM}}/n_{\text{QM}}$, where n_{QM} is the total number of neighbors of the QM atoms and $n_{\text{QM-QM}}$ is the number of such neighbors that are in the QM region themselves. ν is a convenient property for characterizing the relation between the size and the shape of the QM cluster.

For example, atoms inside the QM cluster are coordinated only with other QM atoms, but atoms at the boundary of the cluster are coordinated with both quantum and classical atoms. Thus, a larger compactness for a given cluster size corresponds to a smaller interface area. Using the QM clusters with the largest value of ν allows one to minimize the perturbations of the electronic structure induced by the QM cluster boundary.

It is advantageous to use stoichiometric QM clusters, i.e., those in which the ratio of different atomic types is the same as in the parent compound. In this case, the QM cluster is neutral and the number of electrons is well defined. Nonstoichiometric clusters are charged. The integer number of electrons reflects either excess or lack of electron charge within the cluster, and this excess charge can affect absolute as well as relative positions of the energy levels.

C. Classical environment

The interaction of the atoms in the classical part of region I with each other and with the atoms of region II is described using a classical force field (FF). The FF has two components: the electrostatic or Coulomb interaction, and the short-range non-Coulomb interactions. In the spirit of the shell model,[33] the former is represented using pairs of point charges (Q_{core} and Q_{shell}) that can be associated with each classical ion, while the latter is represented using pairwise and/or many-body potentials, such as the Buckingham-type potential

$$U^{\text{Buck}}(r_{ij}) = Ae^{-r_{ij}/\rho} - \frac{C}{r_{ij}^6}, \tag{1}$$

where r_{ij} is the distance between a pair of atoms. Parameters A, ρ, and C are fitted, together with the values of Q_{core} and Q_{shell} so as to reproduce known properties of the ideal crystal, including its structure, high- and low-frequency dielectric constants and elastic tensor.

Region I is polarizable, i.e., all centers in this region are allowed to relax. Atoms represented using the shell model contribute to the ionic polarization through their displacements, while the electronic polarization is reproduced by the displacements of the Q_{shell} with respect to the corresponding Q_{core}. The energy cost associated with such displacement is given by $\frac{1}{2}k|\mathbf{r}_{\text{core}}-\mathbf{r}_{\text{shell}}|^2$, where $\mathbf{r}_{\text{core}}$ and $\mathbf{r}_{\text{shell}}$ are the coordinates of the Q_{core} and Q_{shell}, respectively, and k is a fitting parameter related to the electronic polarizability of the system.

To minimize the mismatch between the QM and classical parts of region I, we fitted the parameters of the force field using the following approach. First, the equilibrium lattice parameters of an ideal crystal are calculated using periodic model and the same density functional (for example, B3LYP) and basis sets that will be used in subsequent embedded cluster calculations. Then the force field is fitted so as to reproduce the calculated lattice parameters. By construction, this force field is consistent with the Hamiltonian and the basis set used within the QM cluster. This implies that a new force field needs to be developed for each combination of the density functional and the basis set. In most cases, however, the difference between the corresponding FF parameters is small.

D. Interface region

The interface region is introduced in order to provide a seamless border between the QM cluster and classical ions in region I. The interface atoms perform a dual role: they are considered quantum mechanically along with the atoms of the QM cluster and, at the same time, their interaction with the classical atoms in region I is included via interatomic potentials. Therefore, the parametrization of the interface atoms consists of two parts: (i) an effective pseudopotential $\hat{V}_{\text{Int}}(\mathbf{r})$ for the interaction with the electrons and nuclei of the QM cluster, and (ii) a short-range corrective potential $U(r_{ij})$, which provides the correct potential-energy surface for the interface atoms and their neighbors.

The choice of the pseudopotential $\hat{V}_{\text{Int}}$ depends on the electronic structure of the system. In the case of ionic compounds, such as MgO, the interface Mg ions (Mg^*) can be well represented using large-core semilocal effective pseudopotentials (ECPs).[34] On the other hand, in polar systems, such as SiO_2, $\hat{V}_{\text{Int}}$ should reproduce the ionic-covalent character of the Si-O bond.[19,21]

While $\hat{V}_{\text{Int}}$ is generated so as to provide an accurate representation of the electronic structure at the interface, it may not reproduce the lattice structure satisfactorily. To achieve this, we use a classical corrective potential $U(r_{ij})$, which depends upon the atomic coordinates of the interface atoms and their neighbors only. A procedure used to generate this potential is described in Sec. III.

III. IMPLEMENTATION OF THE EMBEDDED CLUSTER SCHEME FOR *c*-ZrO_2

Small (3–5 nm) cubic and tetragonal ZrO_2 NCs synthesized using different methods often exhibit almost spherical shapes in transmission electron microscopy (TEM) images (see, for example, Refs. 15 and 30). We note that the relation between the shape and size of the NCs and the phase stability of ZrO_2 is nontrivial, as was shown recently in Ref. 35. Below, we describe the details of an embedded cluster model for studying defects in such NC's and present the results for oxygen vacancies in the center of ZrO_2 NCs. However, the same approach could be applied to modeling vacancies anywhere inside an NC as well as for studying different cluster shapes.

Quantum-mechanical calculations carried out in this work use DFT with the B3LYP density functional. There is a general consensus that this functional provides fairly accurate geometrical parameters and electronic structures of both wide-band-gap insulators and semiconductors.[36] To choose the geometrical parameters of *c*-ZrO_2 we first calculated the geometric and electronic structure of a perfect infinite crystal using a periodic model and the CRYSTAL 06 code.[37] The basis set for oxygen atoms was taken from Ref. 38. It includes 14*s*, 6*p*, and 1*d* primitive Gaussians contracted to 1*s*, 3*sp*, and 1*d* shells using an (8/411/1) scheme and has been used previously in studies of a large number of oxides.[38] The standard

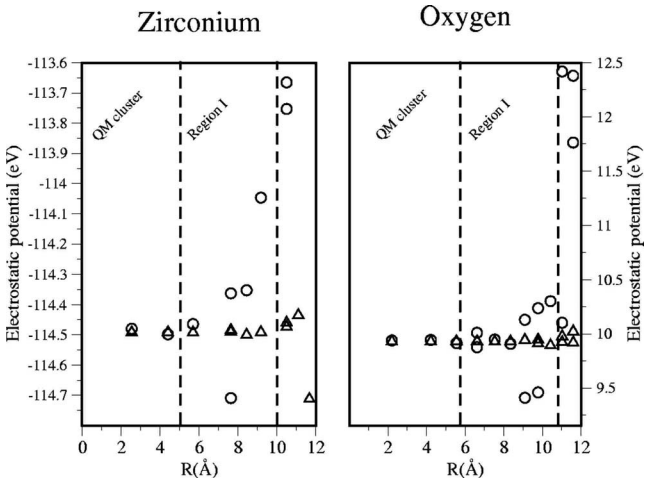

FIG. 2. On-site electrostatic potential inside finite spherical nanoclusters of $R_{NC}=16$ Å (circles) and $R_{NC}=22$ Å (triangles). R is the distance from the center of the nanocluster to a respective lattice site. Dotted vertical lines indicate radius of the QM cluster (~5 Å) and that of region I (~10 Å).

LANL2DZ basis and its corresponding effective core pseudopotential were used for Zr atoms. This basis set consists of 6*s*, 6*p*, and 4*d* primitive Gaussians contracted to 3 *sp* and 2*d* shells using a (411/31) scheme. The calculations were performed for a 96-atom supercell using a Monkhorst-Pack grid of nine k points. The internal coordinates of the supercell were fixed, while the lattice constant was varied so as to minimize the total energy. The value obtained for the lattice constant is 5.07 Å, which is close to the experimental value obtained for the high-temperature cubic phase.

A spherically shaped NC was built using $(\frac{1}{2}\mathrm{Zr})_6(\frac{1}{8}\mathrm{Zr})_8\mathrm{O}_8$ structural units as shown in Fig. 1. It should be noted that Zr atoms are placed on the faces and corners of the structural units, and they will be shared with one and seven other structural units, respectively, in the NC, so they will effectively be considered as 1/2 and 1/8 of atom for the construction of the NC. The choice of this structural element is convenient because it is electrically neutral and has zero dipole and quadrupole moments. Distances between atoms are equal to those in the perfect lattice. This is justified because it has been demonstrated that the interatomic distances in the tetragonal phase NC's are equal to those in bulk samples.[10] Of course, this approach neglects more subtle effects of surface relaxation, which may affect results for small NC's and for defects near surfaces.

Figure 2 shows the on-site electrostatic potential calculated for cubic ZrO_2 NCs of two different radii (R_{NC}). For the $R_{NC}=22$ Å the values of the on-site electrostatic potential inside region I of $R_I=10$ Å are converged to within 0.1 eV. NC of this radius could be also used to study defects in the bulk of cubic ZrO_2. In the following, we use a nearly spherical NC ($R_{NC}=22$ Å), which contains 1570 ions. We note, however, that different procedure could be used to study NCs of some particular shape and size,[39] including optimizing the geometry of the whole NC.

In this work we used a 36-atom QM cluster (shown in Fig. 3), which includes 12 Zr and 24 O atoms. Each of the O

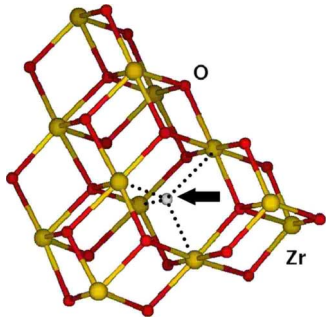

FIG. 3. (Color online) Structure of the embedded QM cluster used in this work. The position of the vacancy in the cluster has been represented with a small sphere connected by dotted lines to nearest-neighbor Zr atoms (marked with an arrow).

atoms in this QM cluster is coordinated by at least two Zr atoms, also considered quantum mechanically. This is the only compact ($\nu=0.48$) average-size QM cluster, which allows us to investigate the electronic structure of oxygen vacancies and local lattice deformation induced by them at a reasonable computational cost. However, structure of ZrO_2 is such that compact QM clusters are usually nonstoichiometric and vice versa. At the same time, if ionic charges in the classical environment deviate from their formal values, the number of electrons that should be assigned to nonstoichiometric QM clusters is not uniquely defined. Therefore, in this study we used formal classical charges (i.e., $+4|e|$ for Zr and $-2|e|$ for O). The effect of this approximation on the electronic structure of ZrO_2 is discussed in Sec. IV B. The electronic structure of the embedded QM cluster is calculated using the B3LYP density functional, as implemented in the GAUSSIAN package,[40] and the same basis set as the one used in the periodic calculation.

The short-range interactions between the classical atoms are described using the Born-Mayer potential $A\exp(-r_{ij}/\rho)$, where parameters A and ρ were developed by Smirnov *et al.*[41] ($A=1610.28$ eV and $\rho=0.34$ Å). Zr ions are represented using a formal ionic charge of $+4|e|$ and they are not polarizable. The O ions are represented using the shell model, with core and shell charges of $+2|e|$ and $-4|e|$, respectively, and a spring constant with a value of $k=200.1$ eV/Å^2.

In order to check the performance of these potentials, we compared the values of different properties of c-ZrO_2 calculated using this set of interatomic potentials with those obtained from different sources (see Table I). Due to the high temperatures required to stabilize bulk c-ZrO_2, measuring these properties for a pure cubic phase is difficult. The lattice parameters and the bulk modulus have been compared with the experimental data available. Elastic moduli have been compared with the data extrapolated from doped phases of c-ZrO_2. No experimental data have been found for the bulk dielectric constant so comparison was made with accurate *ab initio* calculations. In general, the interatomic potential set reproduces correctly the values of the different properties considered, with the largest discrepancy for the values of the dielectric constant and bulk modulus.

In many cases, interatomic potentials may need to be adjusted further in order to reproduce the structural parameters

TABLE I. Comparison of the lattice constants (a), bulk moduli (B_0), elastic constants (C_{ij}), and static dielectric constants (κ) in c-ZrO_2, calculated using the classical interatomic potentials, and values obtained through experiment or periodic *ab initio* calculations.

Property	This work	Other works
a (Å)	5.07	5.09[a]
B_0 (GPa)	328	194[b]
C_{11} (GPa)	684	508[c]
C_{12} (GPa)	150	132[c]
C_{44} (GPa)	47	78[c]
κ	13.3	31.8[d]

[a]Reference 63.
[b]Reference 64.
[c]Reference 65.
[d]Reference 66.

obtained from the periodic calculation, thereby to avoid creating a mismatch between the quantum and classical regions of the embedded cluster model, and to prevent the build up of strain in the system. In this particular case, however, the interatomic distances obtained using the classical model differ only by 0.1% on average from the values obtained using the periodic model, making it unnecessary to refit the parameters.

The interface region between the QM cluster and its classical environment includes all Zr atoms within 5 Å of the QM cluster. In this work, these atoms, denoted by Zr^*, are represented using large-core LANL1 ECPs (Ref. 34) and have no basis functions associated with them. This type of interface proved to be appropriate for ionic materials, such as MgO and CaO. The results below demonstrate that it provides sufficiently accurate results for vacancies in ZrO_2.

We used the following polynomial form for the correcting potential $U(r)$ acting between the interface Zr^* atoms and QM oxygen atoms:

$$U(r_{ij}) = C_1(r_{ij} - R_0)^2 + C_2(r_{ij} - R_0)^3 + C_3(r_{ij} - R_0)^4 + C_4(r_{ij} - R_0)^5, \quad (2)$$

where C_i and R_0 are parameters to be fitted and r_{ij} is the O-Zr^* distance. The parameters of this potential were fitted so as to minimize the lattice distortion at the interface. This is done in two steps: First, we selected one of the oxygen atoms at the boundary of the QM cluster and calculated a potential-energy surface (PES_1) for small displacements of this atom along the direction of its bond to the nearest interface Zr^* atom. Then we calculated a potential-energy surface for equivalent displacements of an O atom along a Zr-O bond *inside* the QM cluster (PES_2). The difference between PES_1 and PES_2 was fitted with the polynomial to obtain the corrective potential. The optimal parameters are $R_0 = 1.54616$ Å, $C_1 = 19.8062$ eV/Å^2, $C_2 = -29.1185$ eV/Å^3, $C_3 = 15.1105$ eV/Å^4, and $C_4 = -2.6660$ eV/Å^5.

We note that the corrective potential and parametrization scheme described above are best applicable to a simple case in which all QM O atoms have the same number and configuration of neighboring quantum-mechanical and ECP atoms. However, this is not the case even in cubic ZrO_2. In particular, in the case of $Zr_{12}O_{24}$ QM cluster, some of the QM O atoms have one, two, or three Zr^* ECP neighbors. Thus, the simple corrective potential $U(r_{ij})$ does not prevent the lattice distortion at the interface completely.

IV. VALIDATION OF THE EMBEDDED CLUSTER MODEL

In order to check the accuracy of our embedded cluster model we compare the atomic structure and electronic properties of the perfect c-ZrO_2 lattice calculated using the embedded cluster and periodic models; we divide the analysis into several areas, detailed below.

A. Geometry

We performed a so-called *perfect lattice test*, in which a defect-free QM cluster is embedded in the defect-free environment and the energy of this system is minimized with respect to the atomic coordinates. If the embedding potential is reproducing the effect of the crystalline environment accurately, there should be no geometry relaxation in this case and the electronic structure of the embedded cluster should correspond well to the electronic structure of the infinite crystal.

In practice, we find that local lattice distortions at the interface are always present, as discussed at the end of Sec. III. However, their magnitude is small and the cubic symmetry of the lattice is maintained. For example, in the case of the embedded $Zr_{12}O_{24}$ QM cluster the angles between the nearest neighbors (nns) change by $\sim 1.0°$ on average. Compared with the reference Zr-O distance of 2.20 Å, the Zr-O bonds in the classical polarizable region remain almost unchanged (the change is below 0.02 Å), while those in the central area of the QM cluster become ~ 0.05 Å shorter. The largest distortions are at the interface itself: Zr_{Int}-O_{QM} are ~ 0.1 Å shorter, while Zr_{Int}-O_{Class} are ~ 0.1 Å longer than the Zr-O reference value.

B. Electronic structure

Figure 4 shows the atom-projected density of states for c-ZrO_2, calculated using both periodic and embedded cluster models. The qualitative features of the electronic structure obtained using both methods are in good agreement with each other, and with results reported previously.[42–44] In particular, the embedded cluster calculation predicts a single-particle band gap of 6.67 eV. This is larger than the band-gap value found using periodic B3LYP (5.7 eV) and experimental estimates of 5.5–5.8 eV.[42,45] This difference is caused by two factors: (i) the ions of the classical environment are assigned formal charges, which results in an overestimated Madelung potential; and (ii) a relatively small number of atoms in the QM cluster, which leads to underestimated bandwidths of the valence band (VB) and conduction band (CB) and, thus, an overestimated band gap. The band gap obtained for a 12-atom QM cluster is 6.82 eV, larger than the value obtained for the larger cluster. As the charges of the classical atoms are reduced, we observe a small reduction in

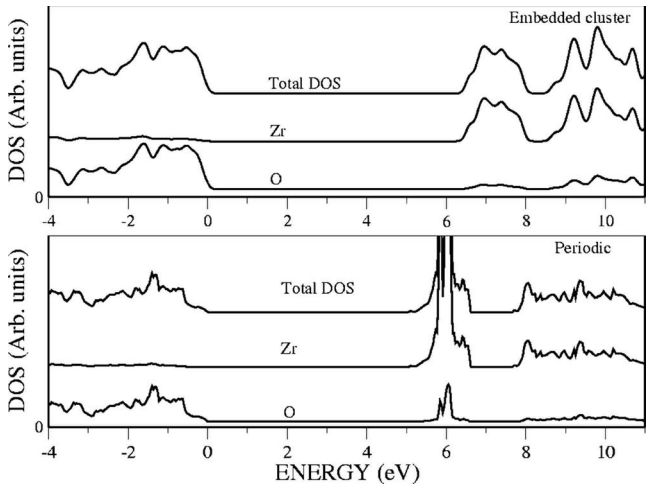

FIG. 4. Atom-projected densities of states (DOSs) calculated using the embedded cluster (top) and periodic (bottom) models. The DOSs are shifted so as the top of the valence band is at 0.0 eV.

the atomic charges in the QM cluster by less than $0.1|e|$ as well as a reduction in the band gap.

The valence band is composed mainly of O $2p$ states with a small contribution from Zr d states, while the conduction band is composed mainly of the $4d$ states of Zr. The detailed structure of one-electron levels calculated using the embedded cluster method matches that of the periodic calculation: states up to 2 eV below the top of the valence band are composed almost exclusively of equivalent linear combinations of O $2p$ orbitals. The bottom of the conduction band is split into two subbands, the lowest one composed of $d(z^2)$ and $d(x^2-y^2)$ states, and the upper one formed from d orbitals of the other symmetries. These bands are split by about 0.7 eV.

C. Charge distribution

The natural orbital population analysis (NPA) of the embedded QM cluster charge density shows that the atomic charges in the QM cluster depend only slightly on their relative positions: Zr atoms near the center of the QM cluster and those at the border have average atomic charge values of $+2.8|e|$ and $+3.0|e|$, respectively. Similarly, average charges of the O atoms are $-1.4|e|$ and $-1.5|e|$ in the central part and the periphery of the QM cluster, respectively. Atomic charges obtained using Mulliken population analysis show a difference of less than $0.1|e|$ from those obtained using NPA. In comparison, the Mulliken charges obtained from the periodic model calculations are smaller: $+2.4|e|$ for Zr and $-1.2|e|$ for O atoms.

V. STRUCTURE AND PROPERTIES OF OXYGEN VACANCIES

Having validated the embedded cluster model for the perfect crystal, we apply this method to one of the most common defects found in ZrO_2: the oxygen vacancy. Oxygen vacancies are usually found in formal charge states of $+2|e|$, $+1|e|$, and $0|e|$, although recent studies in the related oxide HfO_2 suggest that charge states of $-1|e|$ and $-2|e|$ are also possible (see Ref. 25 for an overview). Therefore, here we consider five vacancy charge states: V^{2+}, V^{+}, V^{0}, V^{-}, and V^{2-}. In each case we remove the oxygen atom nearest to the center of the QM cluster to create a vacancy (see Fig. 3) and then minimize the total energy with respect to coordinates of all the centers in region I.

TABLE II. Vacancy-induced displacements of Zr_{nn} atoms from their respective sites in the ideal lattice. Positive and negative values correspond to displacements from and toward the vacancy, respectively.

	Displacements (Å)			
	Zr_1	Zr_2	Zr_3	Zr_4
V^{2+}	+0.20	+0.21	+0.21	+0.20
V^{+}	+0.08	+0.12	+0.12	+0.08
V^{0}	−0.06	−0.04	−0.03	−0.05
V^{-}	−0.08	−0.06	−0.02	−0.19
V^{2-}	−0.10	−0.08	−0.06	−0.20

Changing the vacancy charge state induces changes to its local atomic structure, i.e., causes significant displacements of neighboring atoms, and affects the number and the position of the defect levels in the band gap. For comparison, we also consider such changes for the V^0 and V^{2+} using the periodic model and the same methodology as described in Sec. III for ideal ZrO_2.

A. Local geometry

In the perfect crystal, an oxygen atom is coordinated with four Zr atoms in a tetrahedral arrangement. Our results suggest that that the removal of an oxygen atom to create a vacancy does not produce significant distortions of the tetrahedron formed by neighboring Zr atoms. However, atom-atom distances in the neighborhood of the defect change according to its charge state. Table II shows vacancy-induced displacements of V-Zr_{nn} atoms from their lattice sites in the nondefective lattice. We notice that the Zr_{nn} displacements are almost exactly radial, i.e., either to or away from the vacancy site, and they are symmetrical for the positively charged vacancies and asymmetrical for the negatively charged ones. In particular, in the case of V^{2+}, the four Zr_{nn} atoms displace from the vacancy site by about 0.2 Å or 10% of the Zr-O bond length, which is to be compared with a displacement of 8% obtained using the periodic model. The relaxation is smaller for V^{+}, where the Zr_{nn} atoms displace from the vacancy site by about 0.1 Å or 5% of the Zr-O bond length. In the negatively charged vacancies V^{-} and V^{2-} the displacements of Zr_{nn} vary from atom to atom and range from 1% to 10% of the Zr-O bond length. In the case of V^0, the Zr_{nn} atoms displace toward the vacancy site by about 0.03–0.06 Å, which is similar to the Zr displacements of 0.04 Å in average found in the periodic model calculations. Magnitudes of displacements of other atoms in region I are shown in Fig. 5.

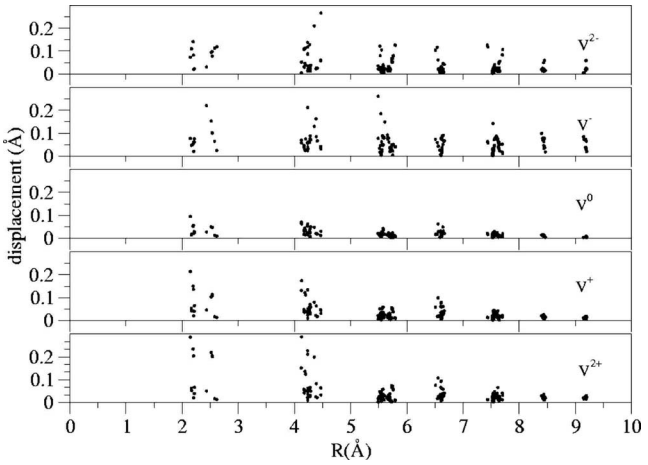

FIG. 5. Vacancy-induced displacements of atoms from their lattice sites. The displacements were calculated for all atoms in region I.

The oxygen atoms in next-nearest-neighbor (nnn) positions from the vacancy site also displace from their original positions: they move toward the positively charged vacancies and away from the negatively charged vacancies. In the case of V^{2+}, the magnitude of these displacements is on the order of 0.2 Å, i.e., about 9% on average with respect to the original Zr-O_{nnn} bond length in both the periodic and cluster models, with two of the eight V-O distances being 0.1 Å shorter than the others. In the other vacancy charge states, the magnitude of the oxygen atom displacements is smaller, ranging between 0.03 and 0.1 Å for V^+ and V^-, and between 0.03 and 0.06 Å for V^{2-}. The displacements in the case of the neutral vacancy are below 0.03 Å.

We notice that the relaxation around the vacancies does not follow the cubic symmetry of the lattice. We attribute this to different factors for different charge states. In the case of the positively charged and neutral vacancies, the slight variations in the displacement of Zr atoms neighboring to the vacancy is due to a choice of the QM cluster, which is nonsymmetrical with respect to the vacancy site (see Fig. 3). In the case of negatively charged vacancies, the extra electrons, "spilled over" from the vacancy site onto the nearby Zr atoms, induce a noticeably large displacement of one Zr atom. A similar effect has been observed in periodic model calculations of cubic HfO_2.[46–48] We attribute it to the tendency of forming one-center electron polarons [discussed earlier for monoclinic HfO_2 (Refs. 25 and 26)], which can be enhanced by the presence of the vacancy.

The spatial extent of the ionic relaxation is closely related to the vacancy charge state. Figure 5 shows the atomic displacements at different distances from the vacancy site calculated for five charge states. In all cases the displacements decrease gradually with the distance from the vacancy, but displacements induced by charged vacancies exceed 0.1 Å at distances of up to 8 Å from the vacancy. The neutral vacancy does not induce a significant relaxation beyond ~2 Å from the vacancy, which corresponds to the first coordination sphere of Zr_{nn} atoms. This shows that the typical supercell sizes used in periodic calculations (on the order of 10 Å) do not account fully for the relaxation effects induced by charged vacancies in this system, and explains the difference in the values of Zr_{nn} displacements calculated using the embedded cluster and periodic models. One can also expect significant variations in the properties of charged vacancies at different positions relative to a NC surface, caused by both electrostatic potential variation and the extent of structural distortion.

TABLE III. Vacancy-induced changes in atomic NPA charges on Zr_{nn} centers calculated with respect to the corresponding values in the ideal lattice. Charge associated with the basis functions positioned at the vacancy site is shown as $Q(V)$.

	$\Delta Q(Zr_1)$	$\Delta Q(Zr_2)$	$\Delta Q(Zr_3)$	$\Delta Q(Zr_4)$	$Q(V)$
V^{2+}	+0.13	+0.08	+0.07	+0.12	−0.01
V^+	−0.09	−0.07	−0.08	−0.09	−0.14
V^0	−0.33	−0.27	−0.27	−0.30	−0.21
V^-	−0.44	−0.43	−0.38	−0.59	−0.22
V^{2-}	−0.59	−0.58	−0.47	−0.69	−0.22

B. Charge distribution

The charge-density distribution around the vacancies has been analyzed using the NPA method and compared to that in the defect-free system (see Table III). In the case of V^0, nearly 1/3 of the electron charge is transferred from the vacancy to each of its Zr_{nn} neighbors. This reduces to $\sim 0.1|e|$ in the case of V^+. For the doubly charged V^{2+}, we find the opposite effect: Zr_{nn} atoms become more positive than they are in the ideal crystal. In the case of negatively charged vacancies the electron charge spills over from the vacancy to the Zr_{nn} atoms, similarly to the V^0 case. Such delocalization of the electron density over nn cations has also been observed in HfO_2.[25] Comparative analysis of the spin-density distributions in V^+ and V^- also suggests that the excess electrons are not confined to the vacancy: the spin density occupies the center of the vacancy in V^+, while in V^- it is located in three of the four nearest-neighbor zirconium atoms; this difference in the character of electron localization is reflected in the relaxation pattern around positively charged and negatively charged vacancies. Interestingly, the electron charge associated with the basis set of the vacancy is nearly the same in V^0, V^-, and V^{2-}.

C. Electronic structure

Vacancies in ionic compounds induce the formation of localized electron levels, located in the band gap or inside the valence and conduction bands. Detailed analysis of these levels sheds light on the electronic and optical properties of these defects. However, comparing the relative positions of these states in the energy diagram is not a trivial task, as different charge states of the vacancy may produce nonnegligible differences in the band gap of the cluster. To locate the levels induced by the vacancy in each calculation, we used as a reference the lowest energy state corresponding to the conduction band. This choice allows us to relate the position of a particular localized level with the correspond-

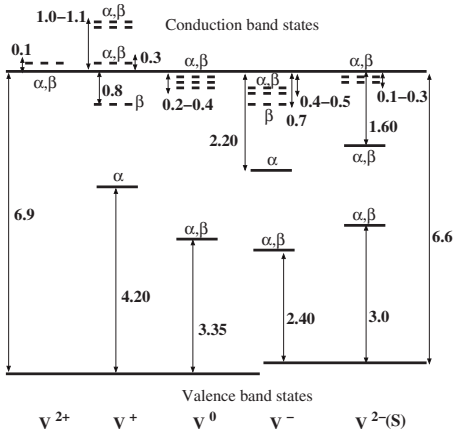

FIG. 6. One-electron defect level diagram for oxygen vacancies in c-ZrO_2, calculated using the embedded cluster method. Continuous lines refer to occupied levels, while dashed lines correspond to unoccupied levels. α and β symbols mark spin-up and spin-down one-electron states, respectively.

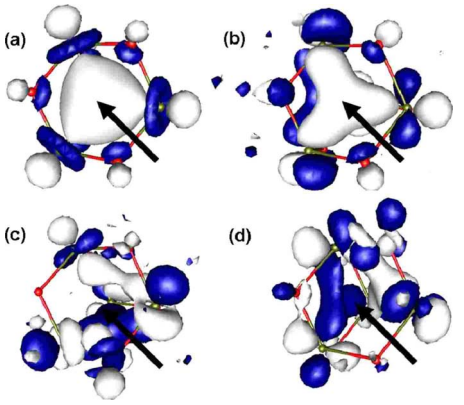

FIG. 7. (Color online) Isosurface representation (value $=0.047$ e Å^{-3}) of one-electron states associated with the neutral oxygen vacancy in c-ZrO_2: (a) the doubly occupied midgap state; [(b)–(d)] unoccupied resonant states inside the conduction band (shown in the order of increasing energy). Zr and O atoms are shown with bright and dark spheres, respectively. The vacancy site is indicated with an arrow on each state.

ing optical transition from this level to the conduction band.

In this location procedure it is important to differentiate resonant levels in the conduction-band states from true conduction-band states; the position and number of the former depends on the charge state of the vacancy. In the case of oxygen vacancies in c-ZrO_2, the resonant states are much more localized than the conduction-band states, and a simple inspection of the contributions of the different atoms to the orbitals of these states is enough to pinpoint them.

One-electron energy levels calculated for the oxygen vacancies in c-ZrO_2 are shown in Fig. 6. The first interesting feature to note is the absence of V^{2+}-induced defect levels in the gap. The level corresponding to this charge state is about 0.1 eV higher than the lowest unoccupied molecular-orbital (LUMO) state; the corresponding state has an approximately spherical symmetry, and it is composed mainly of Zr d contributions from the nearest neighbors with some small contribution from the next-nearest-neighbor O atoms.

V^+ and V^0 centers produce a series of one-electron levels in the gap and in the conduction band. Positions of these levels are shown in Fig. 6. The occupied defect level is located in the middle of the gap, at 2.7 and 3.5 eV, below the bottom of the conduction band. As in the V^{2+} case, this state has approximately spherical symmetry [see the isosurface of the wave function of this state in Fig. 7(a)], and it is formed from a combination of d orbitals from the nearest-neighbor Zr atoms and next-nearest-neighbor O atoms, although in this case the contribution of the O states is larger.

A V^+ center also produces an unoccupied spin-down level in the upper region of the gap, 0.8 eV below the conduction-band minimum (CBM), of the same symmetry as the spin-up state in the middle of the gap. These defects also create resonant states in the conduction band. Three states, located 0.3, 1.0, and 1.1 eV, above the CBM were found for V^+. The same number of states, although located 0.4, 0.3, and 0.2 eV below the CBM, were found for V^0. The symmetry of the wave function for these three states is shown in Figs. 7(b)–7(d). It can be observed that in these states the s-like shape of the vacancy state is replaced by combinations of d orbitals of the nearest-neighbor Zr atoms that surround the vacancy position but do not fill it.

The negatively charged vacancies produce a group of localized levels similar to those produced by the neutral vacancy, with the following modifications. First, the midgap level observed in V^0 lowers its energy by about 0.7 eV in V^- and by 0.1 eV in V^{2-}. Second, one of the vacancy-induced localized levels near the CBM becomes occupied and drops to 2.2 eV in the case of V^- and to 1.6 eV in the case of V^{2-}. Third, several localized states are created in the CBM region: two α-spin states and one β-spin state in the case of V^-, and two doubly occupied states in the case of V^{2-}. No resonant states have been observed in higher-energy regions of the conduction band for these two charge states.

To investigate the effect of the lattice relaxation on the energies of the localized levels, we considered V^+ and V^- centers and restricted the lattice relaxation to the two neighboring shells of QM atoms. The resulting nn-cation displacements are similar to those obtained in fully relaxed systems, but the nnn-oxygen displacements are smaller. However, the positions of the one-electron levels are strongly affected. In particular, the midgap and upper-gap levels of V^+ are 0.9 and 0.5 eV, respectively, lower than in the case of the fully relaxed geometry. On the other hand, the midgap and upper-gap levels of V^- are both 0.4 eV higher in energy.

To study the effect of QM cluster size, we performed a calculation of V^0 in a model with a smaller QM region, consisting of four Zr ions and seven O ions surrounding the vacancy. In this model, the geometry relaxation around the vacancy is similar to that observed in the previous model, with displacements of Zr_{nn} ions around 0.03 Å toward the vacancy site and displacements of about 0.01 Å of the O_{nnn} ions. Due to small number of atoms the band gap is increased to 8.3 eV, which is almost 2 eV larger than in the large cluster case. The middle-gap occupied level is split by 3.6 eV from the valence-band maximum (VBM). The resonant levels are split by between 0.8 and 0.5 eV from the CBM, which is about 0.3 eV lower than in the large-cluster

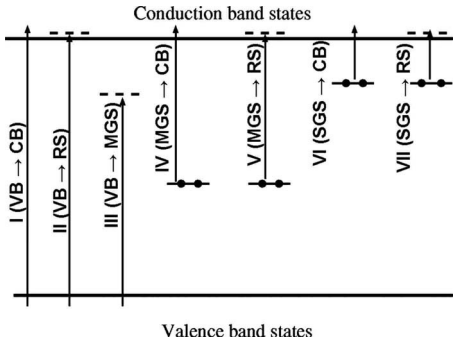

FIG. 8. Optical transition types for oxygen vacancies in c-ZrO_2: (I) band-to-band transitions, (II) VB to resonant state transitions, (III) VB to unoccupied vacancy levels in the gap transitions, (IV) middle-gap state to CB transitions, (V) middle-gap state to resonant state transitions, (VI) shallow-gap state to CB transitions, and (VII) shallow-gap state to resonant state transitions. Note that resonant states in the embedded cluster calculations are split from the CBM.

case. These results indicate that using a small QM region may lead to large errors in determining the band gap of the system.

D. Optical and magnetic properties

Accurate calculations of spectroscopic characteristics such as the optical-absorption spectrum and EPR g tensor are very important for the identification of defects and, in this particular case, can help to determine which charge states of the oxygen vacancy can be present in c-ZrO_2 NCs. Within our embedded cluster scheme these properties are straightforward and relatively inexpensive to calculate.

In particular, optical transitions in c-ZrO_2 with an oxygen vacancy can be classified into seven types, as illustrated in Fig. 8. Band-to-band transitions (type I in Fig. 8) in the perfect lattice cluster begin at 6.0 eV. The excitation energies of these transitions are almost unaffected by the charge state of the vacancy and range from 5.95 eV in V^{2+} to 6.05 eV in V^0. Transitions involving the localized levels created by the presence of the vacancy are shown in Table IV. It can be seen from the table that almost all charge states of the vacancy present transitions around 2.5 eV, corresponding to type V transitions, and transitions between 5.0 and 5.7 eV corresponding to type III transitions. Transitions around 3.2 eV may correspond to either type V for V^+ or type IV for negatively charged vacancies. Transitions below 1.0 eV, correspond to type VI and are only present in V^- and V^{2-}.

TABLE IV. Optical-absorption energies (in eV) calculated for oxygen vacancies in c-ZrO_2. Only most intense transitions are included. The nature of each type of transition is shown in Fig. 8.

	V^{2+}	V^+	V^0	V^-	V^{2-}
Type II	6.00	6.31			
Type III		5.25	5.66	5.02	5.53
Type IV		2.02	2.77	3.38	3.25
Type V		2.54, 3.20, 3.40	2.47	2.84	2.86
Type VI				0.78	0.29
Type VII					

We have also calculated the g tensor for paramagnetic V^+ and V^- centers. The obtained principal values are $g_1=1.946$, $g_2=1.949$, and $g_3=1.961$ for V^+, and $g_1=1.898$, $g_2=1.945$, and $g_3=1.972$ for V^-.

VI. DISCUSSION AND CONCLUSIONS

We implemented the embedded cluster model for the study of cubic nanocrystalline zirconia and calculated the electronic structure and properties of oxygen vacancies. Five vacancy charge states, from $+2|e|$ to $-2|e|$, have been analyzed, and the spectroscopic properties of these charge states have been calculated in order to provide guidance to possible experimental measurements.

Comparison of the theoretical results with experimental data for c-ZrO_2 is not easy, as measurements on bulk samples can only be performed at high temperatures or with large amounts of doping, and spectroscopic data of cubic NCs have not yet been reported. However, the high symmetry and derived reduced computational cost of *ab initio* calculations on this phase have favored its use as a model for the study of the monoclinic phase. This has been justified by the similarities in the band gap, nature of bands, and, in the case of oxygen vacancies, similar environment around the defect in the two phases[44,49,50] and calculations on interfaces between ZrO_2 and transition metals.[13,51]

In terms of comparison with experimental data, optical-absorption experiments in m-ZrO_2 show a signal at about 2 eV above the VBM attributed to the presence of oxygen vacancies.[43] The closest time-dependent density-functional theory (TDDFT) value in our calculations corresponds to transitions of types IV and V in V^+ and V^0.

The EPR spectra measured for m-ZrO_2 in different conditions[52–56] have been associated with defects. These works report a g tensor with $g(\|)=1.961$ and $g(\perp)=1.976$ values. The identity of these paramagnetic species is still unclear: the main candidates include oxygen vacancies, impurities in the crystal, and Zr^{3+} states. Our calculated values for the g-tensor components of the V^+ center are close to the experimental value, although the symmetry of the g tensor is different.

Comparison with the cation-stabilized cubic phase of ZrO_2 is less straightforward, as the presence of the dopant cation can cause significant modifications of the electronic structure of the material, inducing a different distribution of localized levels in the gap and different spectroscopic features. In addition, evidence of vacancy pairing has been found in both experimental and theoretical studies,[3,4] which can also affect strongly the one-electron spectrum of the stabilized phase with respect to that of the pure cubic phase. *Ab initio* calculations performed so far on this system seem to point to this last feature as being the determining factor in the distribution of the electronic levels of the vacancy in the case of Y- and Ca-stabilized zirconia, as the contribution of these cations to the states in the gap region is negligible.[3,57]

Studying the properties of defects in stabilized phases is beyond the scope of this paper (see Ref. 58 for more discus-

sion). Nonetheless, there are hints suggesting that the single-vacancy c-ZrO_2 model can grasp some of the physics of the yttrium-stabilized phase. In particular, EPR measurements on yttrium-stabilized zirconia after electroreduction or radiation processes[59–61] exhibit a signal with $g(\perp)=1.972$ and $g(\parallel)=1.996$ that has been attributed to a V^+ center and is close to our theoretical estimate for V^+. In addition, samples irradiated with low-energy ions[61,62] show absorption bands at 2.44 and 3 eV; the first value has been proposed to correspond to neutral oxygen vacancies or V^+ centers. Our calculated type IV and V transitions for V^+ and V^0 agree with this value.

ACKNOWLEDGMENTS

This work was funded by the EPSRC-GB (Grant No. GR/S80080/01) and the Grant-in-Aid for Creative Scientific Research (Grant No. 16GS0205) from the Ministry of Education, Culture, Sports, Science and Technology of Japan. Computer time was provided by the Computational Resource Allocation Group (CRAG) at University College London. D.M.R. would like to thank K. Hermansson and her research group for their hospitality and financial support during his stay at Uppsala University. P.V.S. was supported by the Royal Society of Great Britain and WPI-AIMR, Tohoku University.

[1] *High-k Gate Dielectrics: Why Do We Need Them?*, edited by M. Houssa (IOP, Bristol, 2004).

[2] *Materials Fundamentals of Gate Dielectrics*, edited by A. Demkov and A. Navrotsky (Springer, The Netherlands, 2005).

[3] G. Stapper, M. Bernasconi, N. Nicoloso, and M. Parrinello, Phys. Rev. B **59**, 797 (1999).

[4] A. Bogicevic, C. Wolverton, G. M. Crosbie, and E. B. Stechel, Phys. Rev. B **64**, 014106 (2001).

[5] S. Fabris, A. T. Paxton, and M. W. Finnis, Acta Mater. **50**, 5171 (2002).

[6] F. Namavar, G. Wang, C. L. Cheung, R. F. Sabirianov, X. C. Zeng, W. N. Mei, J. Bai, J. R. Brewer, H. Haider, and K. L. Garvin, Nanotechnology **18**, 415702 (2007).

[7] G. Garnweitner, L. M. Goldenberg, O. V. Sakhno, M. Antonietti, M. Niederberger, and J. Stumpe, Small **3**, 1626 (2007).

[8] M. Gateshki, V. Petkov, G. Williams, S. K. Pradhan, and Y. Ren, Phys. Rev. B **71**, 224107 (2005).

[9] D. G. Lamas, A. M. Rosso, M. Suarez Anzorena, A. Fernandez, M. G. Bellino, M. D. Cabezas, N. E. Walsoe de Reca, and A. F. Craievich, Scr. Mater. **55**, 553 (2006).

[10] S. Shukla and S. Seal, Int. Mater. Rev. **50**, 45 (2005).

[11] M. W. Pitcher, S. V. Ushakov, A. Navrotsky, B. F. Woodfield, G. Li, and B. Boerio-Goates, J. Am. Ceram. Soc. **88**, 160 (2005).

[12] J. M. McHale, A. Auroux, A. J. Perrotta, and A. Navrotsky, Science **277**, 788 (1997).

[13] A. Christensen and E. A. Carter, J. Chem. Phys. **114**, 5816 (2001).

[14] R. H. R. Castro, P. J. B. Marcos, A. Lorriaux, M. C. Steil, L. Gengembre, P. Roussel, and D. Gouvea, Chem. Mater. **20**, 3505 (2008).

[15] M. Forker, P. de la Presa, W. Hoffbauer, S. Schlabach, M. Bruns, and D. V. Szabo, Phys. Rev. B **77**, 054108 (2008).

[16] H. T. Zhang, G. Wu, and X. H. Chen, Mater. Chem. Phys. **101**, 415 (2007).

[17] H. Liu, L. Feng, X. Zhang, and Q. Xue, J. Phys. Chem. **99**, 332 (1995).

[18] Y. Zhang, H. Lin, and D. G. Truhlar, J. Chem. Theory Comput. **3**, 1378 (2007).

[19] P. V. Sushko, S. Mukhopadhyay, A. M. Stoneham, and A. L. Shluger, Microelectron. Eng. **80**, 292 (2005).

[20] S. Mukhopadhyay, P. V. Sushko, A. M. Stoneham, and A. L. Shluger, Phys. Rev. B **71**, 235204 (2005).

[21] A. V. Kimmel, P. V. Sushko, and A. L. Shluger, J. Non-Cryst. Solids **353**, 599 (2007).

[22] K. M. Beck, M. Henyk, C. Wang, P. E. Trevisanutto, P. V. Sushko, W. P. Hess, and A. L. Shluger, Phys. Rev. B **74**, 045404 (2006).

[23] J. Carrasco, C. Sousa, F. Illas, P. V. Sushko, and A. L. Shluger, J. Chem. Phys. **125**, 074710 (2006).

[24] J. S. Braithwaite, P. V. Sushko, K. Wright, and C. R. A. Catlow, J. Chem. Phys. **116**, 2628 (2002).

[25] D. Muñoz Ramo, J. L. Gavartin, A. L. Shluger, and G. Bersuker, Phys. Rev. B **75**, 205336 (2007).

[26] D. Muñoz Ramo, A. L. Shluger, J. L. Gavartin, and G. Bersuker, Phys. Rev. Lett. **99**, 155504 (2007).

[27] P. V. Sushko, A. L. Shluger, K. Hayashi, M. Hirano, and H. Hosono, Phys. Rev. Lett. **91**, 126401 (2003).

[28] K. P. McKenna, P. V. Sushko, and A. L. Shluger, J. Am. Chem. Soc. **129**, 8600 (2007).

[29] M. Müller, S. Stankic, O. Diwald, E. Knozinger, P. V. Sushko, P. E. Trevisanutto, and A. L. Shluger, J. Am. Chem. Soc. **129**, 12491 (2007).

[30] G. Clavel, M.-G. Willinger, D. Zitoun, and N. Pinna, Eur. J. Inorg. Chem. **2008**, 863 (2008).

[31] P. V. Sushko, A. L. Shluger, and C. R. A. Catlow, Surf. Sci. **450**, 153 (2000).

[32] P. V. Sushko, A. S. Foster, L. N. Kantorovich, and A. L. Shluger, Appl. Surf. Sci. **144**, 608 (1999).

[33] B. G. Dick, Jr. and A. W. Overhausen, Phys. Rev. **112**, 90 (1958).

[34] P. J. Hay and W. R. Wadt, J. Chem. Phys. **82**, 270 (1985).

[35] A. S. Barnard, R. R. Yeredla, and H. Xu, Nanotechnology **17**, 3039 (2006).

[36] F. Cora, M. Alfredsson, G. Mallia, D. S. Middlemiss, W. C. Mackrodt, R. Dovesi, and R. Orlando, Struct. Bonding (Berlin) **113**, 171 (2004).

[37] V. Saunders, R. Dovesi, C. Roetti, R. Orlando, C. M. Zicovich-Wilson, N. M. Harrison, K. Doll, B. Civalleri, B. Bush, and P. L. M. D'Arco, *CRYSTAL 06 User's Manual* (University of Torino, Torino, 2006).

[38] M. D. Towler, N. L. Allan, N. M. Harrison, V. R. Saunders, W. C. Mackrodt, and E. Apra, Phys. Rev. B **50**, 5041 (1994).

[39] P. V. Sushko, J. L. Gavartin, and A. L. Shluger, J. Phys. Chem. B **106**, 2269 (2002).
[40] M. J. Frisch, G. W. Trucks, H. B. Schlegel *et al.*, GAUSSIAN 03, Revision C02, Gaussian, Inc., Wallingford, CT, 2003.
[41] M. Smirnov, A. Migorodsky, and R. Guinebretiere, Phys. Rev. B **68**, 104106 (2003).
[42] R. H. French, S. J. Glass, F. S. Ohuchi, Y.-N. Xu, and W. Y. Ching, Phys. Rev. B **49**, 5133 (1994).
[43] L. K. Dash, N. Vast, P. Baranek, M.-C. Cheynet, and L. Reining, Phys. Rev. B **70**, 245116 (2004).
[44] J. Robertson, K. Xiong, and B. Falabretti, IEEE Trans. Device Mater. Reliab. **5**, 84 (2005).
[45] M. Houssa, M. Tuominen, M. Naili, V. Afanas'ev, A. Stesmans, S. Haukka, and M. M. Heyns, J. Appl. Phys. **87**, 8615 (2000).
[46] K. Xiong, J. Robertson, M. C. Gibson, and S. G. Clark, Appl. Phys. Lett. **87**, 183505 (2005).
[47] K. Xiong, J. Robertson, and S. J. Clark, Phys. Status Solidi B **243**, 2071 (2006).
[48] J. Robertson, K. Xiong, and S. J. Clark, Phys. Status Solidi B **243**, 2054 (2006).
[49] B. Kralik, E. K. Chang, and S. G. Louie, Phys. Rev. B **57**, 7027 (1998).
[50] A. S. Foster, V. B. Sulimov, F. Lopez Gejo, A. L. Shluger, and R. M. Nieminen, Phys. Rev. B **64**, 224108 (2001).
[51] J. L. Beltran, S. Gallego, J. Cerda, and M. C. Muñozi, J. Eur. Ceram. Soc. **23**, 2737 (2003).
[52] S. Wright and R. C. Barklie, Mater. Sci. Semicond. Process. **9**, 892 (2006).
[53] V. Ramaswamy, B. Tripathi, D. Srinivas, A. V. Ramaswamy, R. Cattaneo, and R. Prins, J. Catal. **200**, 250 (2001).
[54] Q. Zhao, X. Wang, and T. Cai, Appl. Surf. Sci. **225**, 7 (2004).
[55] H. W. Liu, L. B. Feng, X. S. Zhang, and Q. J. Xue, J. Phys. Chem. **99**, 332 (1995).
[56] C. Morterra, E. Giamello, L. Orio, and M. Volante, J. Phys. Chem. **94**, 3111 (1990).
[57] F. Pietrucci, M. Bernasconi, C. Di Valentin, F. Mauri, and C. J. Pickard, Phys. Rev. B **73**, 134112 (2006).
[58] D. Muñoz Ramo and A. L. Shluger, J. Phys.: Conf. Ser. **117**, 012022 (2008).
[59] R. I. Merino, V. M. Orera, E. E. Lomonova, and S. K. Batygov, Phys. Rev. B **52**, 6150 (1995).
[60] J.-M. Costantini, F. Beuneu, D. Gourier, C. Trautmann, G. Calas, and M. Toulemonde, J. Phys.: Condens. Matter **16**, 3957 (2004).
[61] J.-M. Costantini and F. Beuneu, J. Phys.: Condens. Matter **18**, 3671 (2006).
[62] D. Simeone, G. Baldinozzi, D. Gosset, S. LeCaer, and L. Mazerolles, Phys. Rev. B **70**, 134116 (2004).
[63] W. C. Mackrodt and P. M. Woodrow, J. Am. Ceram. Soc. **69**, 277 (1986).
[64] A. Dwivedi and A. N. Cormack, Philos. Mag. A **61**, 1 (1990).
[65] S. L. Dole, O. J. Hunter, and C. J. Wooge, J. Am. Ceram. Soc. **60**, 488 (1977).
[66] X. Zhao and D. Vanderbilt, Phys. Rev. B **65**, 075105 (2002).